

SEISMIC SLOPE FAILURE MODELLING USING THE MESH-FREE SPH METHOD

N. Hiraoka¹, A. Oya¹, Ha H. Bui², P. Rajeev² and R. Fukagawa¹

¹Department of Civil Engineering, Ritsumeikan University, Japan;
²Department of Civil Engineering, Monash University, Australia

ABSTRACT: In the past few decades, majority of dynamic behavior of slope have been conducted using the finite element method (FEM). However, earthquakes often cause large deformation and post-seismic soil deformation which are difficult to predict using the FEM due to mesh distortion issues. As an alternative numerical method, the smoothed particle hydrodynamics (SPH) has been recently applied to geotechnical field and showed to be a promising numerical technique to handle large deformation and post-failure behavior of geomaterials. In this paper, taking into consideration of this advantage, the SPH method is applied to simulate response of a slope subjected to seismic loading. Reliability of SPH results was assessed by comparing with experimental data available in the literature. It is shown that the SPH method could qualitatively predict slope failure behavior observed in the experiment.

Keywords: Dynamic analysis, seismic deformation, SPH, slope failure, elasto-plastic analysis

1. INTRODUCTION

Seismic induced lateral displacement in a slope is traditionally determined by Newmark's sliding block approach in design and assessment [1]. However, this method has limitations because of its simplicity. Nowadays, FEM (Finite Element Method), DEM (Distinct Element Method) [2] and FDM (Finite Difference Method) are used to simulate the co-seismic and post-seismic deformation of a slope subjected to seismic load. However, FEM and FDM methods have some disadvantage such as mesh distortion due to large deformation induced by soil failure. DEM, which is based on continuum mechanics, is favorable to simulate large deformation. However, DEM is computationally expensive to simulate the large problem. Moreover, it is quite difficult to specify DEM parameters for contact models.

Alternatively, the mesh-free smoothed particle hydrodynamics (SPH) [3] has been applied to dynamic analysis of geomaterials [4] and shown that the method can be used effectively to predict the large deformation due to soil failure such as slope failure. In this paper, the SPH method is used to study the seismic behavior of a slope. The co-seismic slope displacements and failure surface are calculated and compared with laboratory experimental results. The soil behavior is modeled with the elasto-plastic Drucker-Prager model. The artificial time history is used to simulate the earthquake loading. The seismic loading is applied to the slope by enforcing the motion of the model boundaries.

2. SIMULATION APPROACH

2.1 Soil constitutive model in SPH

As stated, soil is modeled using the elastic-plastic Drucker-Prager constitutive model. The implementation of this soil model in the SPH framework was already presented by Bui et al. [5]. The key equation used to represent the advance soil stresses are summarized here for brevity. The stress-strain relationship of Drucker-Prager's model with non-associate flow rule can be written as follow,

$$\frac{d\sigma^{\alpha\beta}}{dt} = 2G\dot{\epsilon}^{\alpha\beta} + K\dot{\epsilon}^{\gamma\gamma}\delta^{\alpha\beta} - \dot{\lambda} \left(9K \sin \psi \delta^{\alpha\beta} + \frac{G}{\sqrt{J_2}} s^{\alpha\beta} \right) \quad (1)$$

with the rate of change of plastic multiplier $\dot{\lambda}$,

$$\dot{\lambda} = \frac{3\alpha K \dot{\epsilon}^{\gamma\gamma} + (G/\sqrt{J_2}) s^{\alpha\beta} \dot{\epsilon}^{\alpha\beta}}{27\alpha_\phi K \sin \psi + G} \quad (2)$$

where G is the elastic shear modulus; K is the elastic bulk modulus; $\dot{\epsilon}$ is the deviatoric shear strain tensor; $\dot{\epsilon}$ is the elastic strain tensor; ψ is the dilatancy angle; δ is the Kronecker's delta; s is the deviatoric shear stress; J_2 is the second invariants of stress tensor; and α_ϕ is the Drucker-Prager's constant. These equations are discretized with SPH as following,

$$\frac{d\sigma_i^{\alpha\beta}}{dt} = \sigma_i^{\alpha\beta} \dot{\omega}_i^{\beta\gamma} + \sigma_i^{\beta\gamma} \dot{\omega}_i^{\alpha\gamma} + 2G_i \dot{\epsilon}_i^{\alpha\beta} + K_i \dot{\epsilon}_i^{\gamma\gamma} \delta^{\alpha\beta} - \dot{\lambda}_i \left(9K_i \sin\psi \delta^{\alpha\beta} + \frac{G_i}{\sqrt{J_{2i}}} s_i^{\alpha\beta} \right) \quad (3)$$

$$\dot{\lambda}_i = \frac{3\alpha_\phi K_i \dot{\epsilon}_i^{\gamma\gamma} + (G_i / \sqrt{J_{2i}}) s_i^{\alpha\beta} \dot{\epsilon}_i^{\alpha\beta}}{27\alpha_\phi K_i \sin\psi + G_i} \quad (4)$$

where i indicates a particle under consideration. $\dot{\epsilon}$, $\dot{\omega}$ are the strain rate and spin rate tensors, respectively, which are discretized as below,

$$\dot{\epsilon}_i^{\alpha\beta} = \frac{1}{2} \left(\sum_{j=1}^N \frac{m_j}{\rho_j} (v_j^\alpha - v_i^\alpha) \frac{\partial W_{ij}}{\partial x_i^\beta} + \sum_{j=1}^N \frac{m_j}{\rho_j} (v_j^\beta - v_i^\beta) \frac{\partial W_{ij}}{\partial x_i^\alpha} \right) \quad (5)$$

$$\dot{\omega}_i^{\alpha\beta} = \frac{1}{2} \left(\sum_{j=1}^N \frac{m_j}{\rho_j} (v_j^\alpha - v_i^\alpha) \frac{\partial W_{ij}}{\partial x_i^\beta} - \sum_{j=1}^N \frac{m_j}{\rho_j} (v_j^\beta - v_i^\beta) \frac{\partial W_{ij}}{\partial x_i^\alpha} \right) \quad (6)$$

where $j = 1, 2, \dots, N$ are particles in the influence domain of a certain particle i . W indicates function of approximation so-called “kernel function”. The particle position is finally determined as follows,

$$\frac{dx_i^\alpha}{dt} = v_i^\alpha \quad (7)$$

Further details about SPH framework for soil can be found in [5] and [6].

2.2 Boundary conditions and earthquake loading

Accuracy and stability of computation depend on the boundary conditions. In this paper, two types of boundary condition are considered: free-roller and full-fixity. Details of these boundary conditions and their inclusion of seismic motion are discussed in the following section.

2.2.1 Free-roller boundary with seismic motion

Free-roller boundary condition is usually used to represent a far field boundary condition. At the free-roller boundary, soil particles are free to move in the direction which is parallel to the wall boundary. In SPH, the free-roller boundary can be simulated using ghost particles which are placed symmetrically on the opposite side of the wall boundary as shown in Fig.1. The stress boundary condition is set as follow [5],

$$\sigma_G^{\alpha\beta} = \begin{cases} \sigma_R^{\alpha\beta} & \text{if } \alpha = \beta \\ -\sigma_R^{\alpha\beta} & \text{if } \alpha \neq \beta \end{cases} \quad (8)$$

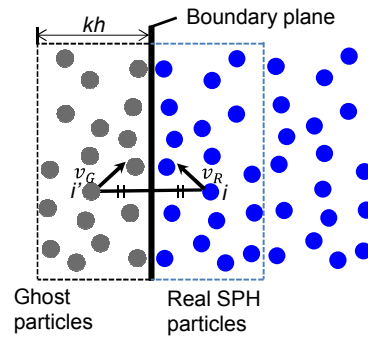


Fig.1 Arrangement and treatment of ghost particles

where σ_G and σ_R are the stress tensor of ghost and real SPH particles, respectively. The velocity of ghost particles v_G is represented as follows [5-6],

$$v_G = \begin{cases} -v_R + 2v_{wall} & \text{if } v_G \text{ is normal velocity} \\ v_R & \text{if } v_G \text{ is shear velocity} \end{cases} \quad (9)$$

where v_R is the velocity of real particles and v_{wall} is used to represent moving wall. In this paper, the seismic wave velocity on the roller boundary is enforced through v_{wall} . In addition, the roller boundary is also subjected to motion according to the seismic motion input.

2.2.2 Full-fixity boundary with seismic motion

The second type of boundary condition which is often used to restraint soil motions at the solid boundary is the full-fixity boundary. In SPH, the fully-fixity boundary condition can be modeled using “boundary particles” which are placed outside the wall boundary as shown in Fig. 2. These particles are normally fixed in the space and carry the same material properties as soil particles [5-6], except the velocity. In this paper, the same approach presented by Bui et al. [5-6] which can be dated back to the original work proposed by Morris et al. [7] is applied. Accordingly, velocity of boundary particles are updated using the following equation,

$$v_{AB} = v_A - v_B = \bar{\beta} v_A \quad (10)$$

$$\bar{\beta} = \min \left(\bar{\beta}_{max}, 1.0 + \frac{d_B}{d_A} \right) \quad (11)$$

where v_A and v_B are the velocity of real and boundary particles, respectively; d_A and d_B are the distance from the real and boundary particles to the wall boundary; and $\bar{\beta}_{max}$ is a constant number which should be chosen to prevent particles getting closer to the wall boundary. In this study, $\bar{\beta}_{max} = 1.5$ is applied based on the recommendation by Bui et al [5].

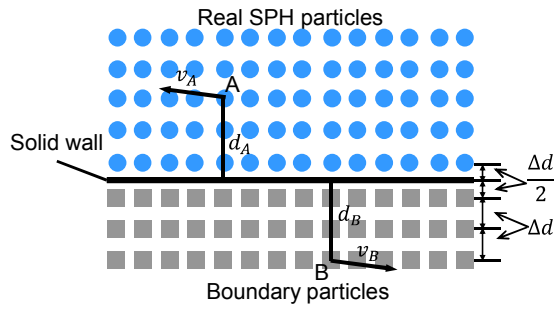


Fig.2 Arrangement and treatment of solid boundary

It is worth noting here that, although boundary particles are assigned with a virtual velocity (v_B), these particles are fixed in the space. However, for the case of moving boundary such as due to seismic motion, equation (10) must be replaced by the following equation,

$$v_{AB} = \beta(v_A - v_{wall}) \quad (12)$$

where v_{wall} is again the seismic velocity wave. As a result, the virtual velocity of boundary particles on the moving boundary can be estimated as follows,

$$v_B = (1 - \beta)v_A + \beta v_{wall} \quad (13)$$

Equation (13) assures that the velocity of real soil particles right at the solid wall will be exactly zero which satisfies the full-fixity boundary condition. However, this boundary condition does not represent the true natural seismic loading condition where the motion of boundary should be applied. In this paper, to simulate the true seismic loading boundary, the boundary particles are subjected to seismic motion which can be obtained by taking integration of the input acceleration.

3. OUTLINE OF EXPERIMENT

A small-scale cut slope shaking table experiment was conducted to verify SPH results. Figure 3 and 4 show the schematic diagram of the experimental setup and the overview of the soil slope shaking table setup respectively. A steel box of 100cm long, 60cm wide and 70cm high was mounted on top of the shaking table. The soil slope model of 90cm length, 60cm width and 50cm height was set in the shaking box, and the slope angle was 45°. The soil used in the experiment was Masa soil which is a weathered granite commonly found at Kansai area in Japan. The particle size over 5mm was eliminated and the water content of soil is set at 10%. The slope was constructed in phases using 5cm thickness compacted layers of 90cm length and 60cm width to achieve the homogeneous soil slope. Finally, the soil

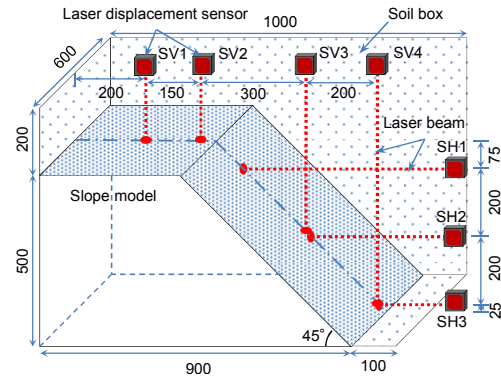


Fig. 3 Outline of the experiment (Unit: mm)



Fig. 4 View of the slope model in experiment

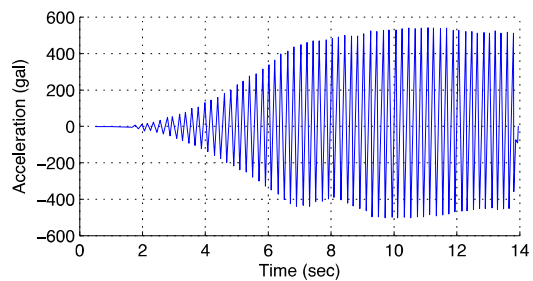


Fig. 5 Acceleration - time history used in experiment

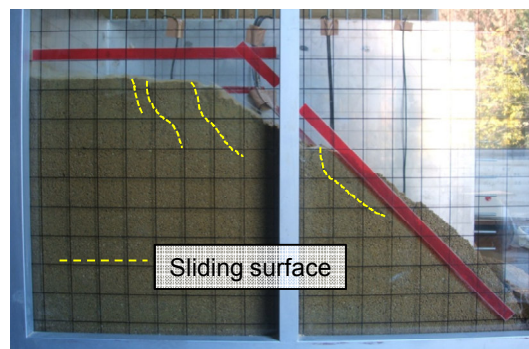


Fig. 6 Final slope configuration after loading

block was shaved to the angle of 45°. The soil parameters are given in Table 1.

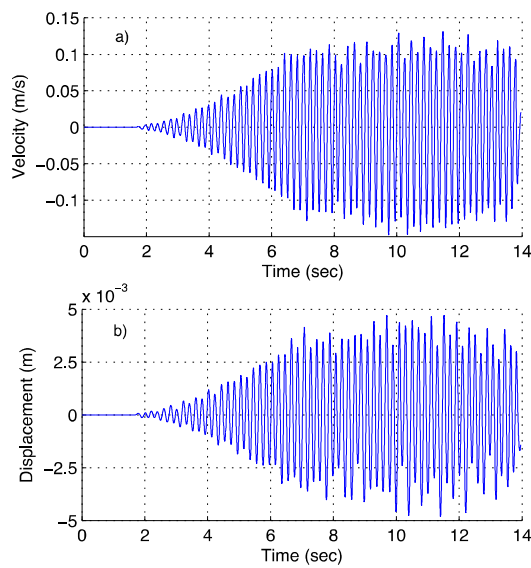


Fig. 7 Input seismic motions: a) velocity and b) displacement

Table 1 Soil parameters

Items	Values	Items	Value
ρ	1.68g/cm ³	ψ	0 - ϕ
ϕ	22.56°	E	2.57MPa
c	0.78 kPa	ν	0.33

To measure displacement within the slope, seven laser displacement sensors were used. Three sensors, named SH1, SH2, and SH3, were fixed to slope side on the soil box to measure horizontal displacement of the slope at given height (see Fig.3). Four laser displacement sensors, named SV1, SV2, SV3, and SV4, were fixed to the top of the soil box to measure vertical displacement at given locations. The shaking table can generate a maximum acceleration of 323m/s² with a corresponding displacement of 5cm in horizontal direction and a frequency of 700Hz.

The slope model was subjected to the seismic wave loading shown in Fig.5, which was recorded from the experiment. Test was run for 14 seconds until the slope was completely collapsed. Figure 6 shows the deformation pattern of the slope at the end of the testing. The top surface of the slope was settled down due to the soil compaction. Four distinct failure surfaces were identified from the side wall, suggesting that the slope was collapsed in several stages during loading. In addition, because the soil slope was constructed on the steel box, the friction at the bottom of the slope is significantly low. Therefore, the sliding along the steel box could also be considered as one of the factors triggering the slope failure.

4. NUMERICAL VALIDATION

A 2D-SPH model was conducted to simulate the

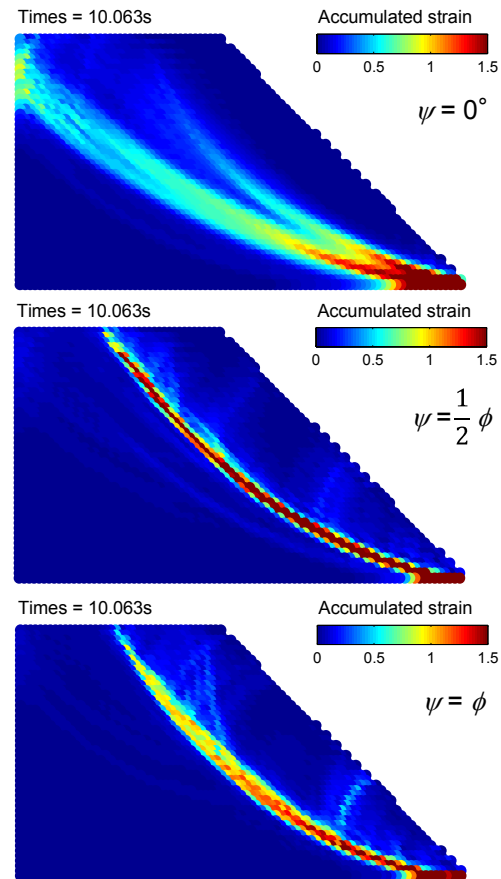


Fig. 8 Effects of dilatancy angle on the failure mechanism.

dynamic behavior of the slope model. Soil parameters for the constitutive model can be found in [7] and summarized in Table 1. The effect of dilatancy angle on the failure mechanism of the slope is investigated. In general, the dilatancy angle can vary from zero to the friction angle. In the case of $\psi = 0$, the plastic volume is constant, and there is no plastic volumetric expansion; however, for the case of $\psi = \phi$, the plastic volumetric expansion is maximal. Therefore, dilatancy angles of $\psi = 0, \phi/2$, and ϕ are adopted throughout this paper. Results of the failure surface and soil displacements are then compared with those observed in the experiment. The effect of pore-water pressure was assumed to be negligible and not considered in this study.

A total of 3245 SPH particles were used to create the slope model shown in Fig.3 with an initial smoothing length of 1.2cm. Boundary conditions are free-roller at the vertical and full-fixity at the base. The initial stress condition in the slope was obtained by applying the gravity loading to soil particles [6]. The slope model was then subjected to the seismic wave loading shown in Fig.7 which was computed from the acceleration time history recorded in the shaking table test. The load was applied by enforcing the seismic motions of the solid wall boundaries.

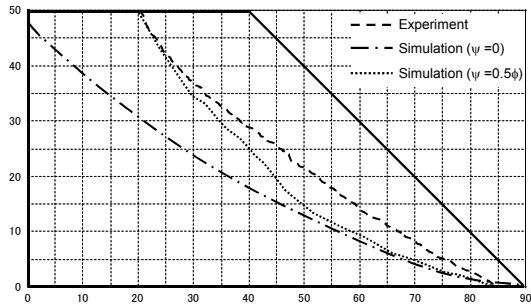


Fig. 9 Comparison between SPH simulation and experiment for the failure surface.

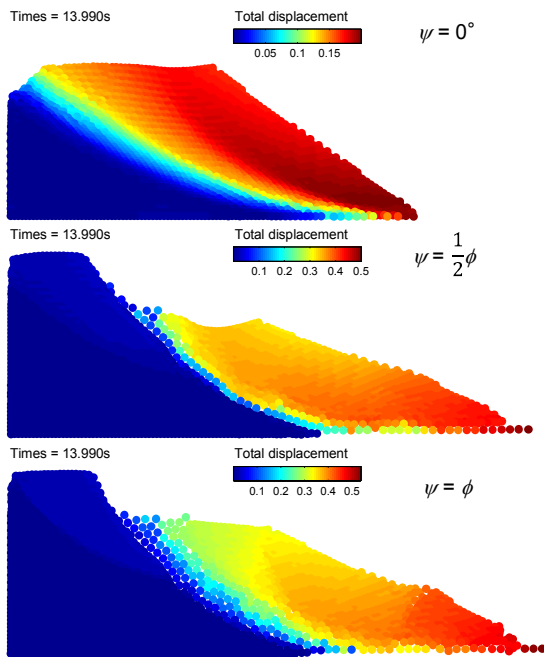


Fig. 10 Effects of dilatancy angle on the post failure behavior of the slope.

Figure 8 shows a comparison of the failure surface obtained in the simulations for different dilatancy angles. The contour plot represents the accumulated deviatoric strain. In the case of $\psi=0^\circ$, soil underwent shear deformation without plastic volumetric expansion, which resulted in the thick shear band layer. Contrarily, when the dilatancy angle was increased, the failure occurred locally due to the development of plastic volumetric strain. As a result, the slip surface was found to be localized in a narrow band.

Figure 9 shows a comparison between experiment and simulation for the failure surface. In the experiment, the failure surface was obtained by removing collapsing soil carefully above the failure surface. It can be seen that the SPH simulation with high dilatancy angle (i.e. $\psi > 0.5\phi$) predicted fairly well the failure surface observed in the experiment. However, the SPH model with ($\psi=0$) overestimated the failure zone. The ends of sliding surface line are

the same in both experiment and simulations. The shape of the sliding surface in the simulation was found to be almost circular, while that of experiment was a curved line having higher curvature angle. It is still not clear about this failure mechanism observed in the experiment because there might have some technical errors when removing the collapsing soil to specify the failure surface in the experiments. Further tests should be conducted to clarify this difference for a future work.

In term of the progressive failure, the experimental results showed that the slope model underwent four failure stages which correspond to four different failure surfaces as shown in Fig.6. The SPH model was unable to reproduce this failure mechanism; however, two failure surfaces were observed in the SPH simulation with ($\psi=0$); while only one failure surface was found in the SPH model ($\psi > 0.5\phi$). On the other hand, the SPH method can simulate well the sliding process of soil after collapse.

Figure 10 shows a comparison of SPH simulations for the post-failure behavior of soil using different dilatancy angles. It can be seen that the higher dilatancy angle is utilized in the simulation, the larger final run-out distance could be predicted in the simulation. This result is conceptually correct and reflects well the behavior of the current constitutive model, that is the larger dilatancy angle is adopted in the constitutive model, the higher plastic volumetric strain could be predicted during the post-yielding process. This result suggests that if a suitable constitutive model is used, the SPH simulation could simulate well post-failure behavior of soil.

Figure 11 shows a comparison between the SPH simulation and the experiment for the vertical and horizontal displacements measured at some specific locations as outlined in Fig.3, i.e. SH1-SH4 and SV1-SV4. In both cases (i.e. $\psi=0$ and $\psi=0.5\phi$), the SPH simulations predicted fairly well the vertical and horizontal displacement profiles measured at different layer displacement sensors. However, simulation results over predicted the final run-out distance of soil measured in the experiment. The SPH model with zero-dilatancy angle seems providing better prediction of the displacement as compared to the SPH model utilizing high dilatancy angle. In addition, it is also noticed that the horizontal displacement at sensor SH1 in the SPH simulation of $\psi=0.5\phi$ went negative, which is significantly different from that observed in the experiment. This can be explained due to the fact the slope collapsed and slid downward along the failure surface. Thus, the measuring location of SH1 in the simulation was no longer on the sliding soil volume, but on the failure surface. This mechanism was however not clear from the experiment. Further research is required to confirm the mechanism.

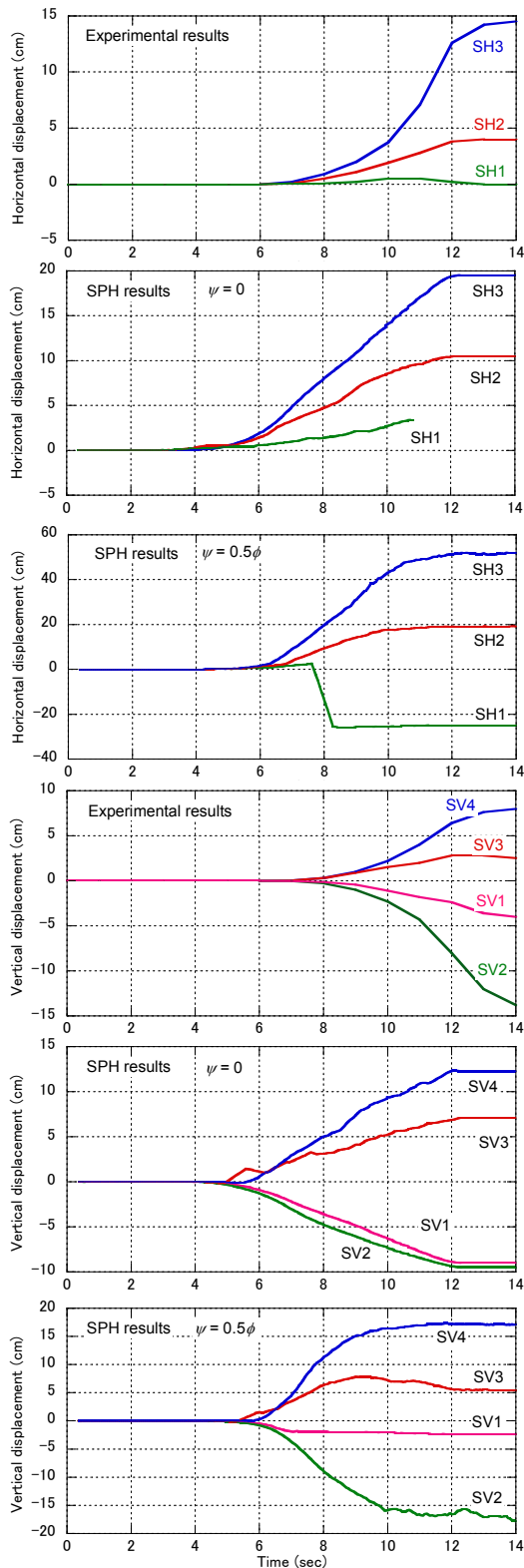


Fig. 11 Comparison between SPH simulation and experiment results for the displacements.

5. CONCLUSION

This study presented the application of SPH to simulate the large deformation and failure behavior

of the slope subjected to dynamic loading. Results showed that SPH predicted fairly well the failure surface observed in the experiment, but significantly overestimated the slope deformation. In order to improve the accuracy of the SPH simulation, advanced soil constitutive model and damping should be taken into consideration. These are the subjects of future work.

6. ACKNOWLEDGEMENTS

This research was supported by the JSPS institution program for young researcher overseas visits.

7. REFERENCES

- [1] Newmark NM, "Effects of earthquake on dams and embankments", *Geotechnique*, Vol 15, No.2, 1965, pp 139-160.
- [2] Cundall PA, Strack ODL, "A discrete numerical model for granular assemblies", *Geotechnique*, Vol 29, Issue.1, 1979, pp 47-65
- [3] Monaghan JJ, Gingold RA, "Smoothing particle hydrodynamics: theory and application to non-spherical stars", *Mon. Not. R. Astr. Soc*, 181, 1977, pp.375-389.
- [4] Bui HH, Fukagawa R, Sako K, Okamura Y, "Earthquake induced slope failure simulation by SPH", *The 5th Int. Conf. Rec. Advanced Geotech. Earthquake Eng., CD*, 2010.
- [5] BuiHH, FukagawaR, Sako K, Ohno S, "Lagrangian meshfree particles method (SPH) for large deformation and failure flows of geomaterial using elastic-plastic soil constitutive model", *Int. J. Numer. Anal. Meth. Geomech*, 32, 2008, pp.1537-1570.
- [6] Bui HH, Fukagawa R, "An improved SPH method for saturated soils and its application to investigate the mechanisms of embankment failure: Case of hydrostatic pore-water pressure", *Int. J. Numer. Anal. Meth. Geomech.*, Vol.37, Issue 1, 2011, pp.31-50.
- [7] Okamura Y, Sako K, Fukagawa R, "Analysis of seismic displacements of slopes applied vibratory conveyance theory", *Journal of JSCE (C)*, Vol.65, No.1, 2009, pp. 162-173.

Int. J. of GEOMATE, Sept., 2013, Vol. 5, No. 1 (Sl. No. 9), pp. 660-665.

MS No. 3318 received on June 26, 2013 and reviewed under GEOMATE publication policies. Copyright © 2013, International Journal of GEOMATE. All rights reserved, including the making of copies unless permission is obtained from the copyright proprietors. Pertinent discussion including authors' closure, if any, will be published in the Sept. 2014 if the discussion is received by March, 2014.

Corresponding Author: N. Hiraoka